Cite this: DOI: 10.1039/c0xx00000x

www.rsc.org/xxxxxx

ARTICLE TYPE

Oxidation Triggered Atomic Restructures Enhancing the Electrooxidation Activities of Carbon Supported Platinum-Ruthenium Catalysts

Po-Chun Huang,[a] Hong-Shuo Chen,[b] Yu-Ting Liu,[c] I-Li Chen,[d] Sheng-Yang Huang,[e] Ha M. Nguyen,[a] Kuan-Wen Wang,[b] Chi-Chang Hu,[d] *and* Tsan-Yao Chen,[a, *]

Received (in XXX, XXX) Xth XXXXXXXXX 20XX, Accepted Xth XXXXXXXXX 20XX
DOI: 10.1039/b000000x

This study demonstrated that the methanol oxidation reaction (MOR) activity of carbon supported Platinum-Ruthenium catalysts (Pt-Ru/C) could be enhanced by 2.6-folds with adequate oxidation treatment. Our results show that such enhancement is triggered by the hetero-junction of Pt atomic layers atop tetragonal phased RuO_2 crystal. At freshly prepared sample, the nanocatalysts (NCs) were built a Ru rich core capping by a PtRu alloy shell. The thermal treatment restructures the Pt and Ru atoms to form the ordered heterojunction at core-shell interface and optimize the activity of NCs at a temperature of 520K. The higher temperature oxidizes the Ru into crystallite rutile RuO_2 phase. In such cases the Pt atoms were segregated to form individual crystallites by a substantial lattice mismatch between metallic Pt and RuO_2 phases. This work presents the systematic analysis with theoretical modelling and quantitative characterizations on manipulating the structural evolutions and thus optimizing the MOR activity of Pt-Ru/C catalysts.

Introduction

The bimetallic platinum-M NPs is regarded as the key factor in green technology for future energy. One typical example is their application in direct methanol fuel cell (DMFC), which employs the methanol electrooxidation reaction (MOR) to generate electricity.[1-10] However, the high cost associated with platinum limits it tangible use in electrochemical devices. In the meantime, during MOR, the reaction sites of NPs would be poisoned by the surface retentions of CO and carbonaceous byproducts (e.g., R-$C_xH_{2x}O$ *etc*).[11]

An effective way to improve the power efficiency and the lifetime of catalysts is to regenerate the poisoned sites.[12] The regeneration can be conducted by adding hydrophilic elements,[2, 12] varying oxidation treatments,[13] controlling the particle size,[1, 14, 15] and building the core-shell structures in bimetallic NPs.[13, 16-19] Underlying the heterogeneous chemistry principles,[1, 11, 12, 20-26] these approaches are mostly basing on the bifunctional mechanism,[2, 27] the ligand effect,[11, 28] and the near-surface lattice strain.[1-3, 11-13, 15, 18, 25, 26, 29-32]

The near surface hydrophilic alloying and heterogeneous interface have been previously found to be the deciding factors in the electrochemical behaviour of the electrocatalysts.[2, 15, 27, 33] As described in the literature, the surface Ru architectures (island, clusters, and alloy *et al.*) would tend to form ruthenium oxide (RuO_2) and then adsorb substantial amount of surface O (-O^{ads}) and hydroxyl ligand (-OH) chemisorptions in ambient condition.[11, 25, 26, 34] The -O^{ads} would diffuse to neighbour sites. Consequently, a larger Pt-decorated Ru NPs surface are more oxidized than the Ru surfaces in the alloy. The Pt-to-Ru neighbour sites are significantly increased therefore enhances the MOR activity of the catalyst.

Here we present a comprehensive study combining structural, electrochemical, and theoretical characterizations on the incipient wetness prepared Pt-Ru/carbon electrocatalysts oxidized at temperatures ranging from 300 K to 570 K. This method improves the MOR activity of Pt-Ru/C by building a hetero-junction between RuO_2 and Pt atoms.[13, 16, 17] In order to quantitatively elucidate the effects of RuO_2 crystallite hetero-junction, the local atomic structure and chemical distributions in NPs against oxidation temperature (T_o) are investigated by combining results of X-ray absorption spectroscopy (XAS) and X-ray diffraction (XRD) analysis at beamlines of Synchrotron light source.[21-23, 35-38] The proposed model with the restructure mechanisms were further illustrated by using the *ab-initio* density functional theory (DFT) calculation and the temperature programmed decomposition with gas chromatography mass spectroscopy (TPD-GCMS). In addition, the electrochemical performance of the Pt-Ru/C in relation with the oxidation temperature was evaluated.

Experiment

Materials

Platinum (IV) Chloride (PtCl4, 99.8%) was obtained from Merck. Ruthenium (III) chloride hydrate ($RuCl_3.3H_2O$, 99.0%) was obtained from Strem. The H_2SO_4 (99.9%) and HNO_3 (99.9%)

were obtained from Sigma-Aldrich. Mesoporous carbon powder (Vulcan XC-72R, surface area = 230 m^2g^{-1}) was obtained from Fuel Cell Store. All the reactions are conducted in the solvent of distilled water.

Catalyst Preparation and Oxidation

The Pt-Ru/C electrocatalysts were prepared by using solution co-precipitation and gas reduction, followed by oxidation at different temperatures (T_o). To reinforce the NPs interface, the carbon support was modified by acid treatment. In this treatment, a 1000 mg of mesoporous carbon powder added to 50 mL of 30 mM HNO_3 aqueous solution and sonicated at 50℃ for 1 h. The powder was then filtered, washed thoroughly with distilled water, and redispersed in water by sonicating the filter paper for ca. 30s followed by drying at 120℃ for 24 h. After the modification, the carbon powder was dispersed into 30 mL of aqueous solution containing 13 mM $RuCl_3$ and $PtCl_4$ then stirred at ambient condition for 24 h. The Ru^{3+}-Pt^{4+} /carbon powder was collected as before. The as impregnated powder was dried at 320 K for 24 h and then reduced under flowing H_2/N_2 (10/90 vol.) gas at 620 K for 1 h to form the freshly prepared catalyst (Pt-Ru/C-H_2). The final concentration of deposited Pt/Ru complexes was determined to be ~12.8 wt% by ICP-AES analysis. To study further the effects of elevated temperature on the composite, this sample was oxidized under an ambient atmosphere at 300 K, 420K, 370 K, 470 K, 520 K, 550 K, and 570 K for 1 h. We named this series of oxidized samples as Pt-Ru/C-T_o NCs (e.g., Pt-Ru/C-300 denotes the sample being oxidized at T_o = 300 K). Before the structure characterization, the samples were purged by a H_2 gas flow (10 sccm) for 30 minutes to maintain the surface metallic structure.

Catalysts characterizations

The atomic structure, crystal structure, and the chemical composition of Pt-Ru/C catalysts are characterized by XAS, XRD (the wavelength of incident X-ray is set to be 1.5399 Å), high-resolution transmission electron microscopy (HRTEM), and TPD-GCMS combined with thermogravimeteric analysis (TGA), respectively. The MOR activity of these catalysts is determined by linear sweep voltammetry (LSV). Here we will firstly build the crystal structure model by XRD and HRTEM analyses. Then the corresponding local atomic structure was investigated. Combining the obtained structural information from micrometer to atomistic regimes, the mechanisms on the metal to oxide junction affecting the electrochemical activity of NCs will be discussed. The details for the characterization methods and instrumental parameters are given in the electronic supplementary information (ESI).

Results and Discussions

Effects of T_o on the crystal structure evolutions of Pt/Ru/C

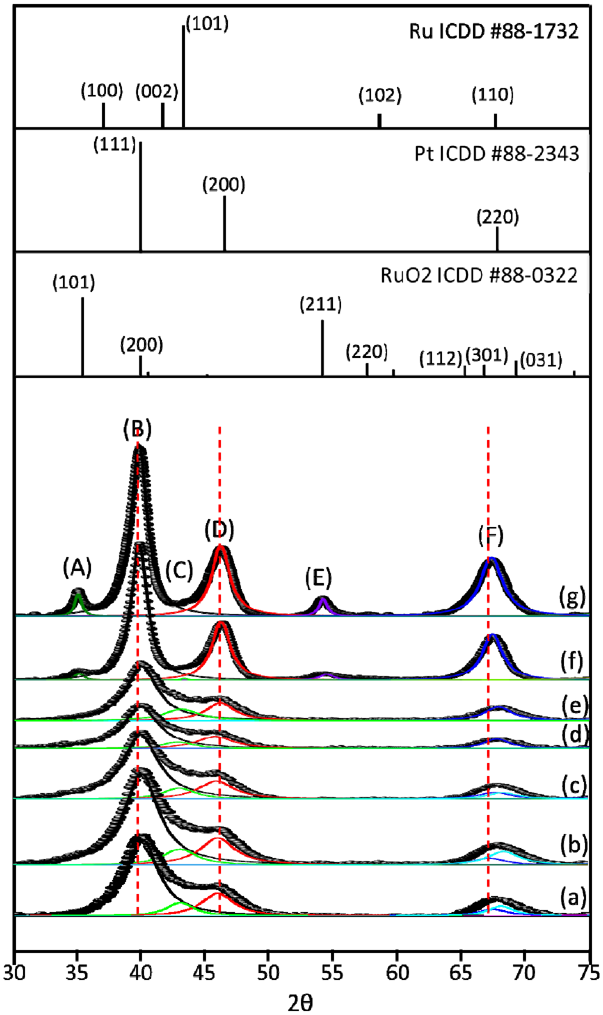

Fig. 1 XRD patterns of Pt-Ru/C catalysts and reference patterns for anhydrous rutile RuO_2 (ICDD #88-0322), metallic Pt (ICDD #88-2343), and metallic Ru (ICDD #88-1732). Where (a) is the pattern of Pt-Ru/C-H2 and that of samples oxidized at (b) 300K, (c) 370 K, (d) 420K, (e) 470 K, (f) 520 K, and (g) 570K, respectively.

Figure 1 shows the XRD patterns for the Pt-Ru/C-T_o samples (oxidized at T_o from 300 to 570 K) comparing with that of standard spectra of Ru (ICDD #88-1732), Pt (ICDD #88-2343), and RuO_2 (ICDD #88-0322) in the upper region. The six peaks from (A) to (F) can be indexed as the diffraction lines from RuO_2 (101), Pt (111), Ru (101), Pt (200), RuO_2 (201), and Pt (220)/Ru (110) facets, respectively. As indicated, the broad peak (B) is found shifted to the higher angle from that of Pt (111). This suggests that the narrowing of interplanar spacing of Pt (111) facets by forming the PtRu nanoalloy in the Pt-Ru/C-H_2 catalyst (see trace (a)). The flattened peaks in XRD spectra (see spectra (b) to (e)) reveal the formation of surface amorphous Pt oxide layer in the NCs been oxidized at a T_o < 470 K. By increasing T_o > 470K (see spectra (f) and (g)), the position of the three main diffraction peaks back shift to that of the metallic characteristic limes of fcc phased Pt accompanied by the formation of peaks (A) (RuO_2 (101)) and (E) (RuO_2 (211)). Such a feature reveals the segregation of PtRu nanoalloy into Pt and Ru domain through the Pt relocation triggered by the exceeding thermal energy followed by the oxidation of Ru into RuO_2 crystallite. This can possibly be attributed to the fact that the substantial lattice mismatch between Pt and RuO_2 and the preferential oxidation of Ru domain, which have been shown to aid in the segregation and restructure of Pt atoms into metallic clusters.[18, 39] On the other hand, the XRD peaks from the platinum oxide are invisible after the segregation has begun shows that the Pt oxide remains in short-range order throughout the oxidation process. Given that the metallic Ru phase is coexisting in the Pt-Ru/C system (see peak (C) in spectra (a) to (e) of **Fig. 1**)[33], the obtained diffraction spectra features illustrating the formation of metallic Ru riched core in hcp phase (D_{avg} = 27.5 Å) capping by a Pt riched shell in fcc phase (D_{avg} = 25.6 Å); where a diffused interface is lying in between.

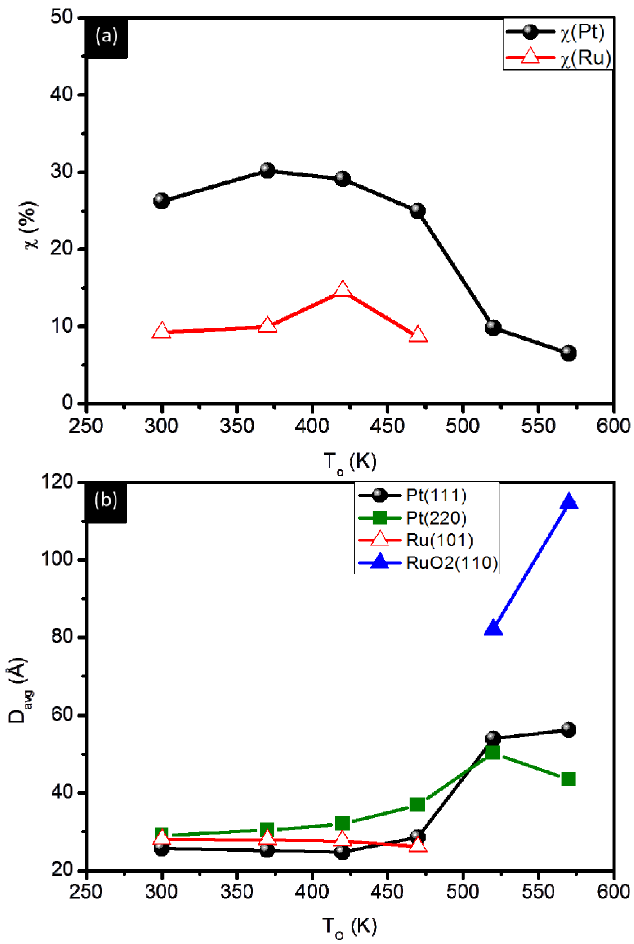

Fig. 2 (a) The extent of heteroatomic alloying for Ru atom in Pt phase (χ(Pt)) and that of Pt atom in Ru phase (χ(Ru)) of Pt-Ru/C nanocatalysts; (b) the average grain size (D_{avg}) of metallic Pt (Pt(111), Pt(220)), Ru (Ru(101)), and Ru oxide (RuO_2 (110) phases determined by Scherer equation.

The corresponding crystal structure parameters including the lattice constant for Pt and Ru phases (see **Table S1**), the extent of heteroatomic alloy for Ru atom in Pt phase (χ(Pt)) and that of Pt atom in Ru phase (χ(Ru)) of Pt-Ru/C NCs (see **Fig. 2a**) are determined by Vegard's law basing on the deconvolution results of Lorentz wave functions for each diffraction peak. Accordingly, the lattice space of Pt fcc phase (i.e., d(111)) of Pt-Ru/C-H_2 was determined to be 2.249 Å which is 0.059 Å larger than that of metallic Ru in fcc phase (see ICDD #88-2333). In this case, according to the solid state solubility theory (Vegard's law), the extent of heteroatomic alloying for Ru atom in Pt domain (χ_{Pt}) is determined to be 26.2%. This heteroatomic alloy is found in a maximum value of 30.2% at T_o = 420 K and then progressively decreasing to a minimum value of 6.5% with increasing T_o till 570 K. The changes of χ_{Ru} with T_o is found in similar track to that of χ_{Ru} (increasing from 9.2% to 14.6% from T_o = 300 K to 420 K and then decreasing to 8.7% at T_o = 470 K). Both the two tracks can be rationalized by the increasing of interface alloying at mild oxidation conditions (at T_o < 420 K) followed by the segregation between the Pt and Ru phases at severe oxidation conditions (at T_o from 420 K to 570 K).

The average coherent lengths (i.e., average grain size, D_{avg}) of the experimental samples are determined by Scherer equation and are shown in **Fig. 2b**. Accordingly, the D_{avg} of metallic Pt (i.e., D_{avg} Pt(111)) and Ru (i.e., D_{avg} Ru(101)) for the sample oxidized at 300 K are determined to be 25.7 Å and 31.8 Å, respectively. Such D_{avg} results are 50% to 60% smaller than that were determined by HRTEM (~ 40 to 50 Å, see **Fig. 3** in latter section), respectively. However this controversial can easily be rationalized by the relative geometric configurations of two the two metallic crystallite phases since the obtained XRD spectra (from trace (a) to (e) in **Fig. 1**) showing the typical diffraction fractures of the core-shell nanoparticles. From this standpoint with the concerns of surface alloying, the high χ_{Pt} than χ_{Ru} suggests the growth of NPs in the Pt riched shell with Ru riched core in the presence of a diffused core-shell interface in the nanoparticle. The changes of metallic Pt D_{avg} at different facets revealing the Pt atom restructure by the external thermal energy. As clearly indicated, no significant D_{avg} Pt(111) changes are found at mild oxidation range (300 K to 470 K) whether the D_{avg} Pt(220) is increased from 30.4 Å to 36.9 Å. Given that the Pt crystallites are growth at the surface of ultra-small Ru nanoparticles with high curvatures and defect densities (given by HRTEM image in **Fig. 3**), such D_{avg} trend can be attributed to the restructure of Pt aatoms from Pt (111) to the surface with high density of open sites (for example Pt(220) facets) in order to minimize the surface free energy of the system. Given that no significant change of D_{avg} Pt(111) was found (see **Fig. 2b**), the decreasing of χ_{Pt} from 30.2 % to 24.9 % again consistently reveals the successive segregation of Ru atoms upon increasing T_o till 470 K. By further increasing T_o from 470 K to 520 K, a substantial drop of χ_{Pt} to 9.8% was found. It indicates the dramatic segregation between Pt and Ru atoms which leading to the formation of RuO_2 nanocrystallite (NC) in rutile phase (proved by peaks (A) and (E) in **Fig. 1**)[17]. In this T_o range, the D_{avg} Pt(111) is increased drastically from 30.8 Å to 54.3 Å because the Pt atoms have a tendency to restructure themselves into monometallic clusters in a presence of driving force providing by the substantial lattice mismatch at heterogeneous surface[21, 36, 39]. Such interparticle sintering is further revealed by the presence of Ru oxide crystallite (i.e., D_{avg} RuO_2 (110)) with the size increasing from 82.1 Å. This segregation further facilitates the interparticle sintering (will be proved by High Resolution Transmission Electron Microscopy (HRTEM) observation in the later sections) and thus triggering a Ru assisted carbon support consumption / combustion (via a Ru-O-C interactions) and is consistently revealed by TPD-GCMS below and in literatures.[13, 19, 40-42] At increasing T_o from 520 K to 570 K, most of metallic Ru was oxidized into RuO_2 (proved by the absence of peak C and the presence of RuO_2 (101), (200), and (211) diffraction peaks). In this T_o range (from 520 to 570 K), RuO_2 D_{avg} (101) was increased from 82.4 Å to 113.9 Å (see **Table S1**). It indicates that the RuO_2 NPs were keep building their long-term structures to minimizing the surface free energy of entire system[43 36].

The proposed T_o impacts on crystal structure evolutions including the present temperature-induced transformation of metallic oxides, the sintering of NCs, and Ru segregations due to Pt restructure are further elucidated via XAS and HRTEM in the later sections.

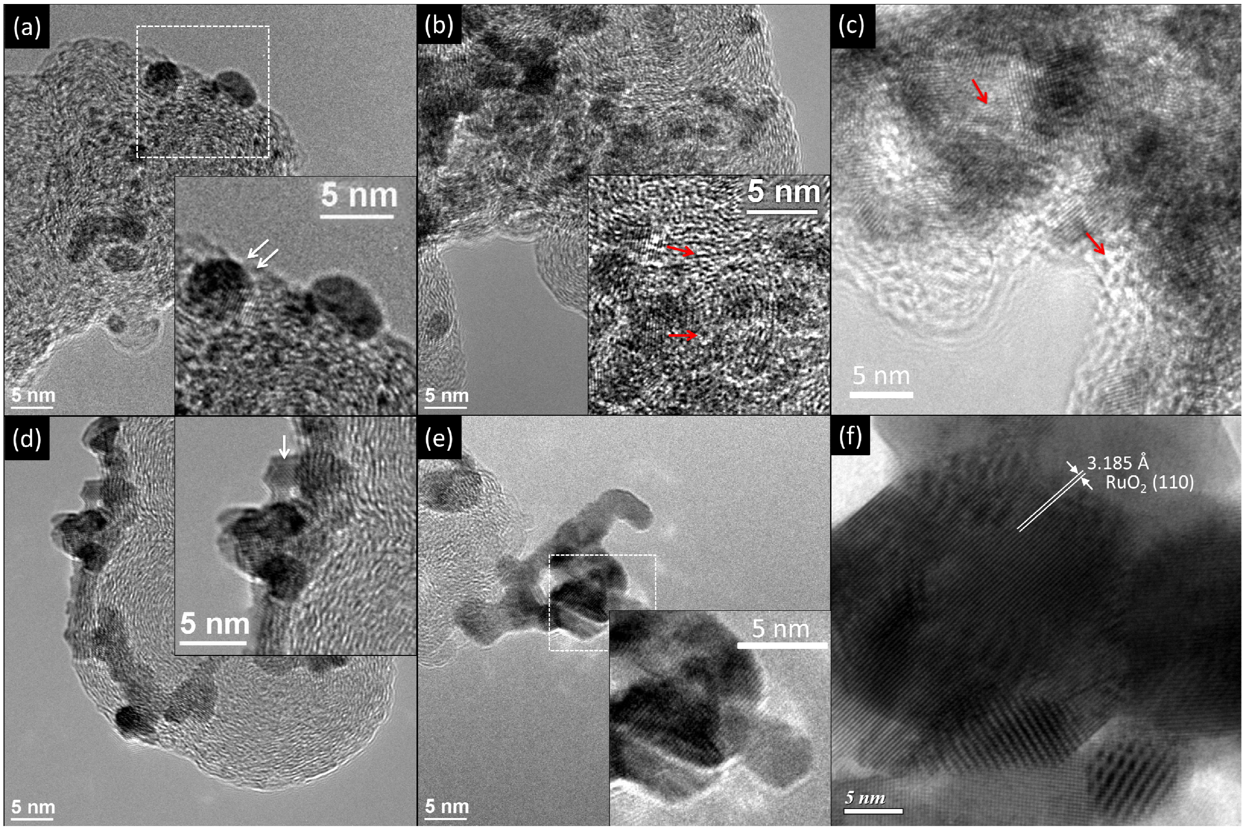

Fig. 3 TEM images of (a) fresh prepared, (b) 370 K, (c) 420 K, (d) 520 K, (e) 570 K, and (f) 600 K annealed Pt-Ru/C catalysts. The corresponding HRTEM images are shown in the insets except (f).

Figure 3 demonstrates the TEM images of the (a) freshly prepared Pt-Ru/C (Pt-Ru/C-H_2) and the samples oxidized at (b) 370 K, (c) 420 K, (d) 520 K, (e) 570 K, and (f) 600 K respectively. As shown in **Fig. 3a**, the NC are grown mostly in a size ranging from 2 to 4 nm and are randomly distributed on the carbon support in the freshly prepared sample. These NCs will then progressively aggregate into clusters by increasing the T_o till 520 K and then further sinter into a large crystallite at specific facets by further increase T_o to 570 K. In this circumstance, the interconnected grain with the average particle size of 7 - 10 nm associating with the decomposition of microporous carbon are found (will be proved by temperature programmed decomposition equipping the gas chromatograph mass spectroscopy (TPD-GCMS) in the later sections. Finally in 600 K sample, the severe sintering and segregation between Pt and RuO_2 (depicted by the lattice fringes of RuO_2 (101) facet with a interplannar spacing of ~3.18 Å in **Fig. 3f**) with carbon decomposition are found, which declaring that the particle sintering could be a result from the RuO_2 assisted carbon combustion at the interface of support. These ranges encompass the NC size estimated from the XRD patterns and the observed microstructure evolution consistent with that depicted by the XRD analysis.

The corresponding high resolution TEM (HRTEM) images are shown in the insects excepting that of **Fig. 3f**. As indicated, the NCs are grown in spherical shape with smeared lattice images. It indicates the formation of long-range disordered f.c.c. phase NC as consistently probed by XRD (in **Fig. 1**, trace g). The substantial aggregation between NC is found by increasing T_o till 420 K. Given that the lattices of NCs are arranging in different orientations (shown by the arrows) the interparticle sintering can be rule out. When T_o at 520 K, formation of interconnected and faceted NC is found at the edge of carbon supports. This suggests the substantial restructure of Pt atoms in their stable phase (i.e., f.c.c. metallic phase) by the thermal driving forces as that were consistently predicted by previous DFT study[36] in the literatures and revealed by the XRD characterizations (**Fig. 1**). It is important to note the formation of core-shell structure in NCs. It forms the intraparticle heterojunction to induce the charge injection / extraction at the particle surface and thus substantially enhancing the MOR activity of the faceted NC (the catalytic performance will be discussed in the electrochemical characterization section). At the high T_o range (570 K to 600 K), the segregation between Pt and RuO_2 phases and the sintering of

NCs are evidently shown in **Fig. 3f** and insect of **Fig. 3e**.

Thermogravimetric (TGA) and temperature programmed decomposition - gas chromatograph mass spectroscopy (TPD-GCMS) analysis

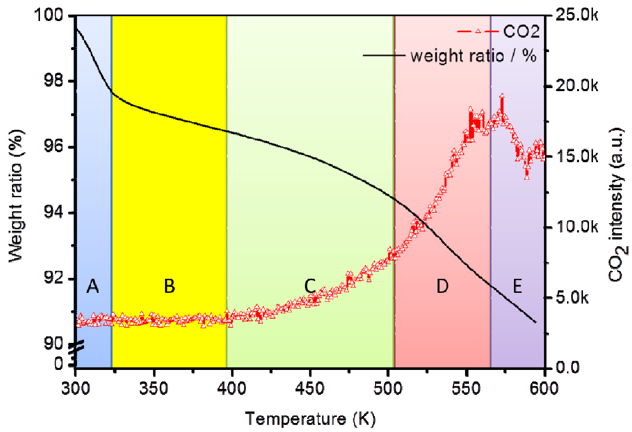

Fig. 4 TGA and TPD-GCMS scans in oxygen for the Pt-Ru/C-H_2 catalyst. Temperature ramp rate was 10 K min^{-1}. The weight loss beginning at ca. 400 K corresponds to loss of carbon support.

To elucidate the role of interactions at heterogeneous interface between carbon support and nanoparticles in the structure evolution of Pt-Ru/C, the temperature dependent TGA combining with the TPD-GCMS were employed (see **Fig. 4)**; where spectrum of blank XC-72 was used as a reference (see **Fig. S5**). Note that the TGA was performed in oxygen, so both decomposition of the carbon and adsorbed species may occur in the same time. Since no significant weight loss of pure XC-72 was found, the weight loss (revealed by TGA scan of Pt-Ru/C-H_2) manifests the carbon decomposition by the presence of bimetallic NPs at a temperature lower than 800 K (see **Fig. S5**). In TPD-GCMS curve, the observed spectrum indicating that the interactions between Pt-Ru NPs and carbon sample can be divided into five different stages (A-to-E) upon increasing temperature from 300 K to 600 K. From 300 K to 320 K (region A), a slight weight loss by 1.7 wt% was observed, which could be assigned to the decomposition / desorption of adsorbed species (e.g., chemisorbed water molecules). There is a gradual weight loss from 320 K to 390 K (region B). Comparing these observations with the changes previously seen in XRD and the CO_2 emission curve, since no CO_2 emission was detected, we suggest that the gradual weight loss below 390 K be associated with a loss of water.[17, 19] Conversely, a significant weight loss was observed from 390 K to 520 K (region C), which could be contributed from the loss of water, the production of CO_2 (decomposition of carbon support), and the increase in crystallinity of the RuO_2.[5, 22, 29, 38, 44, 45] There is an even more drastic weight loss by 4 wt% from 520 K to 570 K (region D). The CO_2 production and PtO_2 decomposition could possibly the main factors in the TGA weight loss. The former is confirmed by the dramatic enhanced CO_2 emission line. This is because if the metallic ions (Ru^{4+} and Pt^{4+}) is being reduced then the adjacent carbon may be oxidized. The later could be triggered by the restructure of Pt atoms into clusters and thus releasing the oxygen molecules (details are given in XAS section). A drastic dip of CO_2 production is found above 570 K (region E). This result, consistent with that of XRD and TEM, could be accounted to the decrease of NPs to carbon contact due to the severe interparticle sintering. Possible reasons for this were discussed in the XRD and XAS results regarding the transition from PtO_2 clusters into metallic Pt.

Effects of annealing temperature on local structure evolutions on Pt-Ru/C

Local chemical states of Pt and Ru atoms

The local structure of experiment catalysts is elucidated by X-ray absorption spectroscopy (XAS). The Ru *K*-edge X-ray absorption near-edge structure (XANES) spectra are shown in **Fig. 5a**. As can be seen, the Pt-Ru/C-H_2 sample XANES spectrum contains two resolved peaks which could be assigned to the metallic characteristics of Ru.[46, 47] The 300 K to 370 K oxidized samples contain one broad peak in the XANES region and closely resemble the features of heavily hydrated RuO_2 samples.[46-48] The further oxidation at 470 K to 520 K would transfer the main Ru species to slightly hydrated RuO_2. The XANES spectrum for the 570 K sample contain a broad peak with a trough in the middle, similar to those seen in literature for anhydrous RuO_2.[48]

Cite this: DOI: 10.1039/c0xx00000x
www.rsc.org/xxxxxx

ARTICLE TYPE

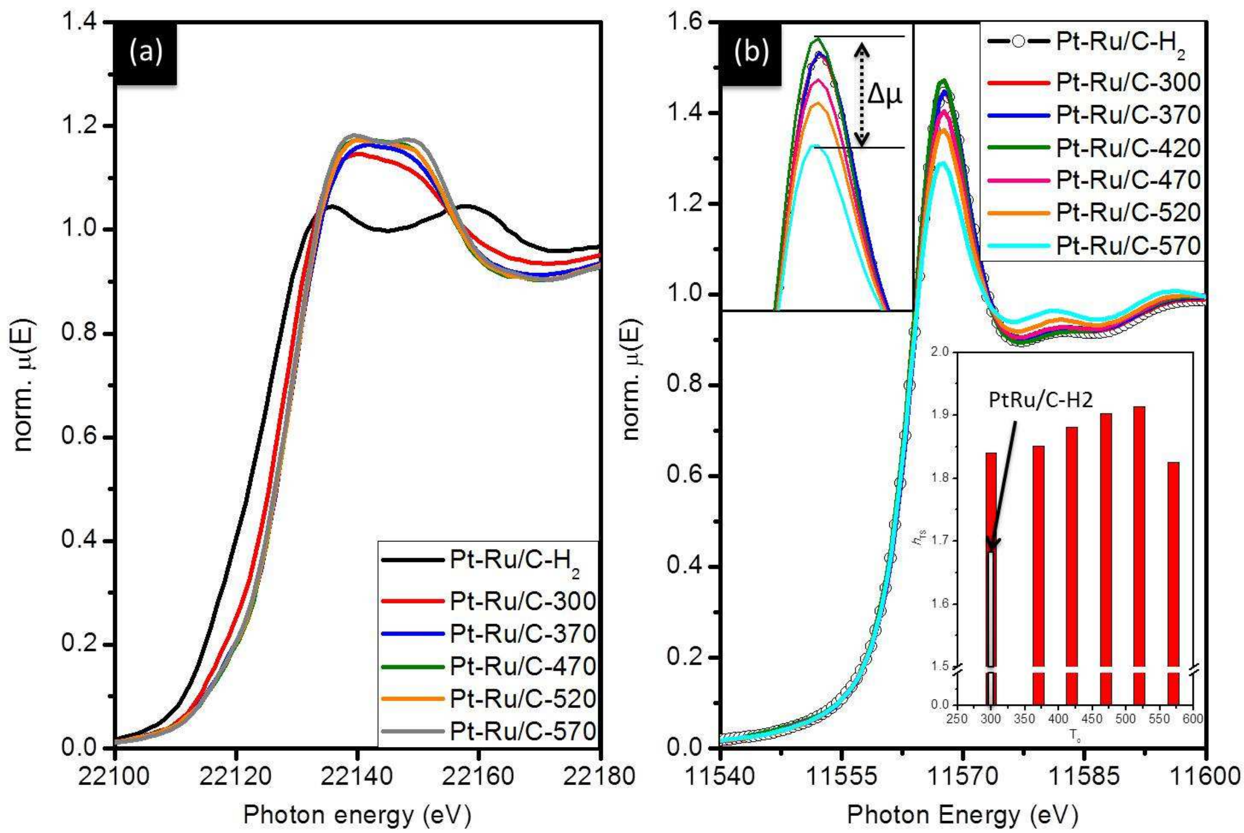

Fig. 5 (a) Ru *K*-edge and (b) Pt L_3-edge XANES spectra of the Pt-Ru/C catalyst oxidized at 300 K to 570 K, respectively. Inset of **Fig.5b** refers to the density of empty states of corresponding samples estimated by L-edges correlation.

The Pt L_3-edge XANES spectra are presented in **Fig. 5b**. As can be seen (the insect of **Fig. 5b** in left hand side), the intensity of white-line (WL) for Pt-Ru/C-T_o samples is found successively increased to a peak value by increasing T_o from 300 K to 420 K and then dropped to a minimum value after further increasing T_o to 570 K (denoted by a WL intensity difference of Δμ). In general, the enhancing WL suggests the increasing charge transition probability from $2p_{3/2}$ to 5d orbitals of Pt atoms (i.e., the increasing empty states at 5d orbital). This feature is a combination factor of the oxidation of Pt atoms and the charge transition from Pt 5d to the hybrid orbital in the neighbouring atoms. Therefore, the decrease of WL intensity along with the narrowing of absorption peak could be attributed to the consequences of the reduced oxygen and dealloying between Pt and Ru phase due to the relocation and clustering of Pt atoms and thus interparticle sintering (also see the results of XRD and HRTEM). To further clarify the weighting factors of the two mechanisms, the effect of T_o on the charge relocation between core-shell interface is elucidated by the number of unfilled d-states of NPs (h_{TS}), which is quantified by a *L*-edges correlation developed by Mansour *et al.*.[49] following an equation (eqn 1):

$$h_{Ts} = (1 + f_d)h_{Tr} \tag{1}$$

where h_{Tr} refers to the number of unfilled d-states of the reference material. The parameter f_d is the fractional change in the total number of unfilled d-states of the NPs compared to the number of the reference foil can be formulated by eqn 2:

$$f_d = \frac{\Delta A_3\,\sigma_3 + 1.11\Delta A_2\,\sigma_2}{A_{3r}\,\sigma_3 + 1.11\,A_{2r}\,\sigma_2} \tag{2}$$

After subtracting the Pt foil data from the NPs data, the resulting curves were then numerically integrated between –10 and 14 eV for both the L_2- and L_3-edges. In the data analysis, the absorption cross sections at the Pt L_3- (σ_3) and L_2-edge (σ_2) were set to be 117.1 and 54.2 $cm^{-2}g^{-1}$, respectively. The variables A_{3r} and A_{2r} denote the integrated area of a standard Pt foil at L_3 and L_2 edges, respectively. The estimated h_{Ts} for the freshly prepared (Pt-Ru/C-H_2) and oxidized samples (Pt-Ru/C-T_o) are summarized in the right hand side inset of **Fig. 5b**. Accordingly, the Pt-Ru/C-H_2 sample gains the minimum h_{TS} and thus the lowest extent of Pt to Ru charge donation among all samples. Such phenomenon could be attributed to the formation of diffused Pt to Ru interface with high extent of structural disordering at near surface region (shown by HRTEM images in **Fig. 3a**). By increasing T_o to 520 K, the h_{TS} is increased to a maximum value. It indicates the strongest extent of Pt to Ru charge donation for Pt-Ru/C-520 among all types of samples. Basing on the heterojunction standpoints, the substantial enhanced Pt to Ru charge donation could be attributed to the increased local structure ordering at their contact region. This hypothesis is shown by the formation of faceted nanoparticle surface and is further revealed by the results of atomic structure analysis in the later sections (EXAFS fitting). On the other hand, a dramatic drop of h_{Ts} is found for 570 K sample and could be the consequence of the substantial de-hybridization between Pt and Ru atoms by restructuring Pt atoms into cluster or large grains as a result of the segregation between Pt and Ru phases (de-alloying).

Local atomic structure around Pt and Ru atoms

Results of atomic structure characterization provide direct evidences for the heteroatomic hybridization in relation with the electrochemical properties of the Pt-Ru/C-T_o. The fits of Ru *K*-edge radial space (R-space) function for the extended X-ray absorption fine structure spectra (EXAFS) are shown in **Fig. 6**. Accordingly, the samples are divided into those containing metallic Ru (freshly prepared sample), orthorhombic RuO_2 NPs (300 K to 370 K), and mixture of monoclinic and rutile RuO_2 (470 K to 570 K). To analysis EXAFS data, the highest quality spectrum (570 K) was fit first to obtain values for the amplitude scaling factor (S_0^2), energy threshold (E_0), coordination number (*CN*), bond distance (*R*), and Debye-Waller factor (σ^2). Then, the other spectra were fit by varying *CN*, R, and σ^2 (with the fixed S_0^2 and E_0 values from the 570 K fits) and these results are given in **Table 1**. Each of the spectra was fit over the *R* range of 1.10 Å to 3.60 Å. The S_0^2 obtained was 0.86, and the E_0 for all scattering path was -6.8 eV. For structure refinements, once the optimum fit was obtained, one parameter was changed until the χ^2 value of the refinement converged. The difference between the value obtained during the fitting and the value at which the χ^2 is the presented uncertainty.[50]

For the case of Pt-Ru/C-H_2, the metallic Ru phase is evident as revealed by the Ru-Ru1 peak across 1.8 - 2.5 Å. The intensity of this radial peak corresponds to an average *CN* of metallic Ru atom in 2.4 (0.6 at 2.14 Å and 1.8 at 2.67 Å). It is important to note that the Ru atoms are highly reactive to oxygen. Hence, the small metallic *CN* implies the formation of short-range-ordered subnano Ru core clusters and the protection of these Ru from oxidation by the surface Pt structure. The radial functions are transformed to the form of orthorhombic RuO_2 by increasing T_o higher than 300 K (depicted by the peak Ru-O1). At 300 K, a weak Ru-Ru1 peak at 2.2 Å (corresponding to a metallic *CN* of 0.2) with the absence of high order Ru-Ru2 radial peaks suggesting the formation of amorphous RuO_2 by a slight of surface oxidation at the Pt-Ru/C-T_o. For 370 K sample, the Ru-Ru1 peak is completely disappeared which is a clear indication for the transition of metallic Ru to heavily hydrated orthorhombic RuO_2 structure from 300 K to 370 K. The fitting results of the Ru-O1 in shell1 indicate that the *CN* of Ru surrounding oxygen atoms is increased to 5.6 with the oxidation temperature to 570 K. Within the temperature range, the 1.22 Å shoulder (peak A) is gradually damped and the Ru-O1 bond distance is elongated. This indicates that the Ru sites were restructured from less symmetric (monoclinic) into highly symmteric (octahedral) geometry by the thermal energy.

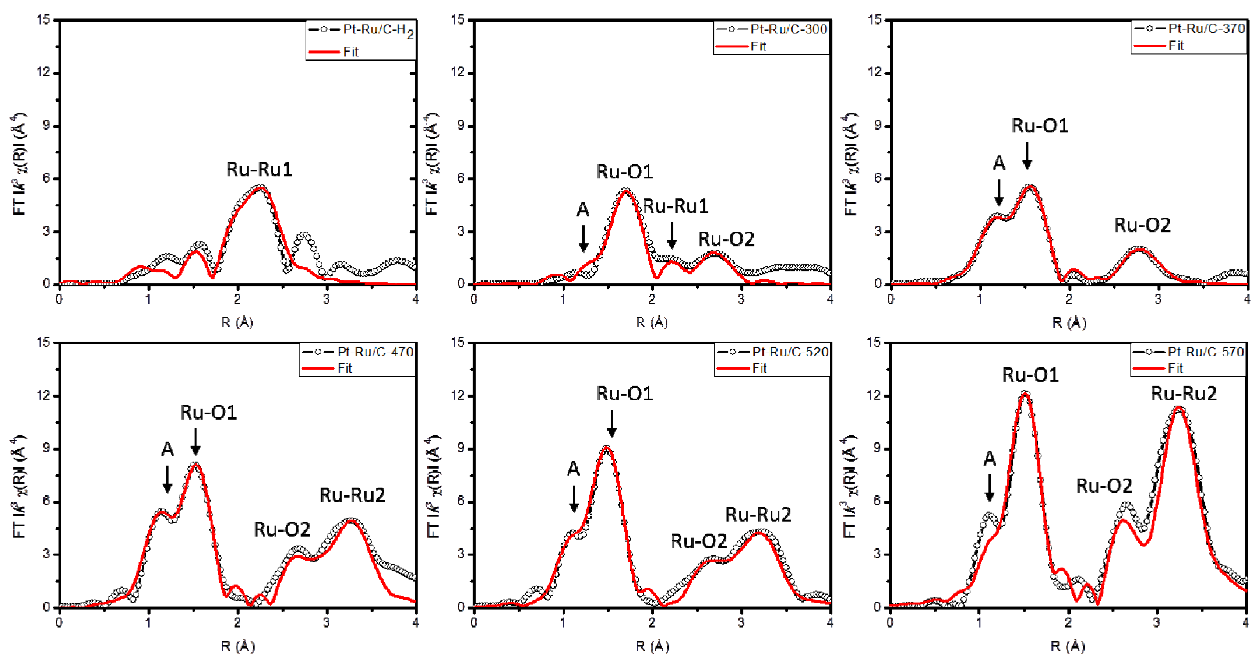

Fig. 6 Ru *K*-edge R-space spectra fits for all Pt-Ru/C catalysts. The open circles are experimental spectra, and the red solid lines are the fits. All spectra were fit from 1.0 Å to 3.6 Å excluding the Pt-Ru/C-H_2.

Cite this: DOI: 10.1039/c0xx00000x

www.rsc.org/xxxxxx

ARTICLE TYPE

Table 1 XAS determined local structure parameters for the Pt-Ru/C-T_o catalysts *

Sample	Pt L_3-edge					Ru K-edge			
	shell1	shell2	shell3			shell1	shell2	shell3	
	Pt-O1	Pt-O2	Pt-PtO	Pt-PtM	Pt-RuM	Ru-O1	Ru-Ru1	Ru-O3	Ru-Ru3
Pt-Ru/C-H_2	1.52 [a]	1.00 [a]	0.45 [a]	0.55 [d]	0.32 [d]	1.42 [e]	0.61 [f]	NA	1.85 [f]
Pt-Ru/C-300	1.45 [a]	0.35 [a]	0.51 [a]	0.60 [d]	0.59 [d]	2.82 [e]	0.21 [f]	NA	0.62 [f]
Pt-Ru/C-370	1.45 [a]	0.35 [a]	0.51 [a]	0.71 [d]	0.66 [d]	3.41 [e]	0.32 [e]	2.23 [e]	NA
Pt-Ru/C-420	1.55 [b]	0.20 [b]	0.51 [b]	0.51 [d]	0.54 [d]	NA			
Pt-Ru/C-470	0.98 [b]	1.20 [b]	0.47 [b]	0.90 [d]	0.59 [d]	4.63 [e]	1.52 [e]	1.22 [e]	2.63 [e]
Pt-Ru/C-520	1.05 [b]	1.20 [b]	0.47 [b]	0.90 [d]	0.65 [d]	5.44 [e]	1.73 [e]	1.81 [e]	3.62 [e]
Pt-Ru/C-570	1.09 [a]	1.78 [d]	0.69 [d]	1.55 [d]	0.58 [d]	5.65 [e]	1.92 [e]	2.72 [e]	5.45 [e]
R (Å)	2.01 - 2.02	2.39 - 2.41	2.61 - 2.76			1.95 - 2.03	[e] 3.13 - 3.14 [f] 2.12 - 2.15	3.31 - 3.43	[e] 3.56 - 3.61 [f] 2.68 – 2.70

*Highest quality fit was obtained with S_o^2 = 0.86. E_o (Pt L_3 - edge) =7.3 eV, and E_0 (Ru K - edge) = 6.8 eV; The sigma square (σ^2) of Pt L_3 and Ru K-edge fitting were determined to be 0.0042 +/- 0.002 and 0.0032 +/- 0.0016 Å^2, respectively.

[a] PtO, SPG 131, Moore, W.J.; Pauling, L., Journal of the American Chemical Society, (1941), 63, 1392-1394; [b] PtO_2, SPG 186, Hoekstra, H.R.;Siegel, S.;Gallagher, F.X., Advances in Chemistry Series, (1971), 98, 39-53; [c] $PtCl_4$, SPG 205, Falqui, M.T., Annali di Chimica (Roma), (1958), 48, 1160-1167; [d] metallic Pt, SPG 225, Davey, W.P., Physical Review (1,1893-132,1963/141,1966-188,1969), (1925), 25, 753-761.; [e] orthorhombic RuO_2, SPG 58, Haines, J.; Leger, J.M.; Schulte, O.; Hull, S., Acta Crystallographica B (39,1983-), (1997), 53, 880-884; [f] metallic Ru

The Ru-Ru1 shell of RuO_2 phase is present in all of the bimetallic samples (excepting Pt-Ru/C-H_2 and 300 K samples), regardless of the oxidation temperature, and is positioned at ca. 3.13 Å - 3.14 Å. This distance is the length of the c axis in the anhydrous RuO_2 unit cell. For the 300 K sample, none of Ru-Ru shells from RuO_2 are found suggesting formation of heavily hydrated RuO_2 NPs. The absence of high order Ru-Ru peaks denotes the formation of disordered RuO_6 octrahedra sites in the orthorhombic RuO_2.[46, 51] The 370 K sample has a Ru-Ru1 *CN* of 0.32 without possessing the second metallic Ru shell contribution. This suggests that the bimetallic NPs containing heavily hydrated subnano RuO_2 clusters. In this case, the presence of 1.22 Å shoulder (A) and the small *CN* of Ru-Ru1 (with the contribution of second Ru-O2 shell in a *CN* of 2.23 across 3.31 Å - 3.43 Å) are indications for the coexistence of monoclinic RuO_2 and the poorly connected chains of disordered RuO_6 octrahedra along the c axis of the unit cell, respectively. The 470 K to 570 K samples have similar local structure to that of RuO_2 NPs in the 370 K sample. However, there is also a contribution from the second Ru-Ru2 shell (at 3.56 Å - 3.61 Å). This peak is attributed to the bond pair between centre and corner Ru atoms in the second coordination shell of rutile RuO_2 unit cell. Therefore, it is suggested that these samples contain considerate extent of bridging between the disordered RuO_6 octrahedra chains. For 520 K sample, the *CN* of Ru-Ru2 (the metallic Ru-Ru bond in shell2) increase to 3.62 indicating that the structure of RuO_2 phase has become much more ordered comparing to that oxidized at temperature below 520 K. As the T_o reaches 570 K, the *CN* approach the values of 1.92 and 5.44 (less than the theoretical value of 2.0 and 6.0 at the 1st and 2nd shells) for the first and second Ru-Ru shells, respectively, suggesting that the structure of the Ru oxide is similar to the anhydrous rutile RuO_2. In this case, the slight negative deviation of *CN* from theoretical value could be evidence showing the formation of locally ordered heterojunction interfaces between Pt and Ru regions. With T_o increasing to 570 K, the growth of rutile by restructuring Ru atoms is noticed by the progressive increasing of high order *CN* and the suppressing of low order Ru-O peak (the shoulder at left hand side of Ru-O1 peak). Also the sharpened R-space peaks reveal the decreasing of σ^2 with an increase in oxidation temperature. This is an indication for the enhanced structure ordering around Ru atoms. However the Ru-Ru *CN* never reach the theoretical values, this suggests that there is a certain extent of disordering present by the enclosure of Pt atoms in the RuO_2 NPs and substantial surface oxides, which are also proved by the Pt L_3 EXAFS results in this study and previous TPR analysis.[13]

Cite this: DOI: 10.1039/c0xx00000x

www.rsc.org/xxxxxx

ARTICLE TYPE

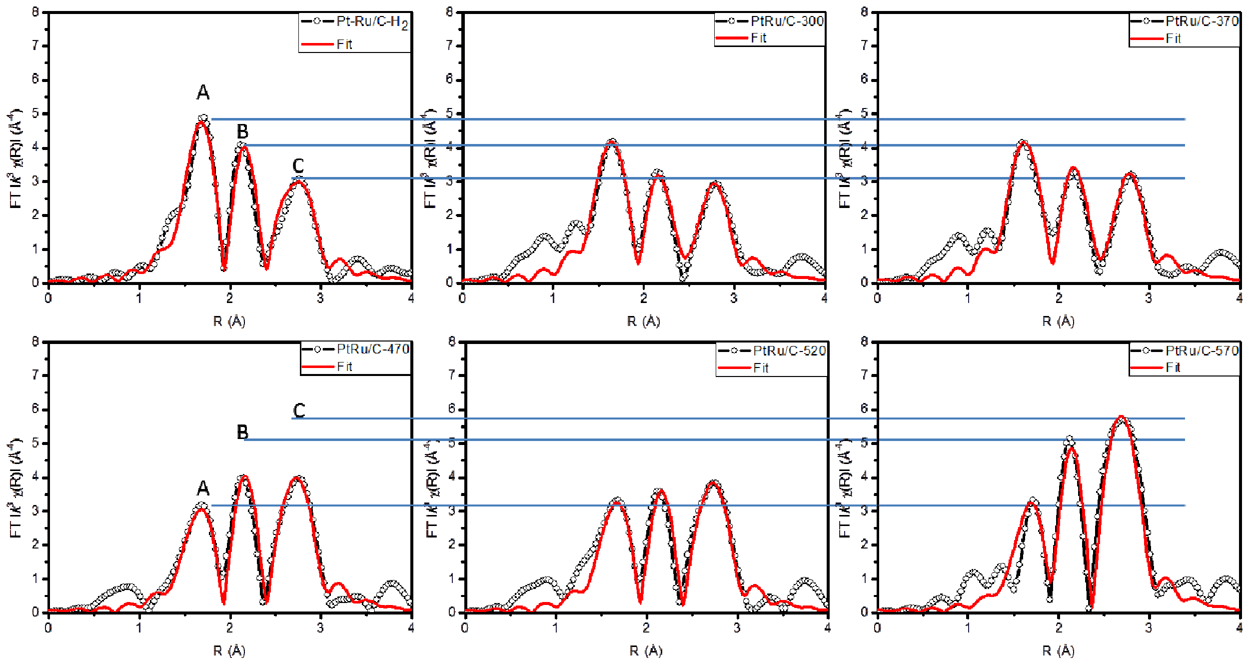

Fig. 7 Pt L_3-edge R-space spectra fits for all Pt-Ru/C catalysts, excluding the Pt-Ru/C-550. The open circles are the experimental spectra, and the red solid lines are the fits. All spectra were fit from 1.1 Å to 3.0 Å.

The fits of Pt L_3-edge R-space spectra are shown in **Fig. 7.** To obtain the quantitative structure parameters a two-phase model consisting metallic PtRu alloy (denoted by peak C with the Pt-PtM and Pt-RuM bond pairs) and PtO_2 (It consists of the peaks A (Pt-O1) and B (Pt-O2) at shell1 and shell2, respectively, and the peak C in part (Pt-PtO) at shell3) phases with different weighting ratios. Each of the spectra was fit over the R range of 1.1 Å to 3.3 Å. The S_0^2 obtained was 0.87, and the E_0 for all scattering path was 7.3eV. Considering that all the spectra were collected under room temperature, the σ^2 value similar to Ru *K*-edge fits was adopted here.

The obtained structure parameters are summarized in Pt L_3-edge column of **Table 1**. As indicated, the all the radial spectra for experiment samples are a convolution functions of PtO_2 and PtRu alloy. In Pt-Ru/C-H_2 the *CN* of for PtO_2 phase at Pt-O1, Pt-O2, and Pt-PtO bonds are determined to be 1.52, 1.00, and 0.45; where that of PtRu metallic phase at Pt-PtM and Pt-RuM bonds are 0.55 and 0.32, respectively. The small *CN* illustrates the coexisting of metallic PtRu and Pt oxides in the sizes within subnano regime. From results of the HRTEM images, these nanoparticles are grown without significant phase separations. Hence, the co-existence of PtO and PtRu alloy suggest a large lattice mismatch between Pt and Ru oxide. For 300 K and 370 K spectra, a substantial drop at Pt-O1 and Pt-O2 intensities (corresponding to the CN decrease of Pt-O1 = 0.07 and Pt-O2 = 0.65) is found indicating the reduction of PtO_2. In addition, a certain extent of CN increase at Pt-PtM (~29%, from 0.55 to 0.71) and Pt-RuM (~106%, from 0.32 to 0.66) are found. These increments depict the formation of local surface alloying at Pt-Ru/C NCs as consistently revealed by XRD analysis (see **Fig. 2b**). At T_o = 470K, a dramatic intensity drop at peak A corresponding to the *CN* decrease of Pt-O1 by 32%, (from 1.45 to 0.98) further elucidates the PtO_2 reduction comparing to the structure parameters of Pt-Ru/C-370. In addition, the *CN* of Pt-PtM is increased by 28% (from 0.71 to 0.90) and that of Pt-RuM is decreased by ~12% (from 0.66 to 0.59) again consistently proving the de-alloying between Pt and Ru phases. For the case of 520 K sample (Pt-Ru/C-520), a slight increase of Pt-RuM *CN* by ~10% (from 0.59 to 0.65) is found, however, that of Pt-PtM remaining unchanged (0.9). Such phenomena can be rationalized by the presence of interparticle necking; where it is expectable to see a local heteroatomic diffusion between Pt and Ru atoms at the core-shell interface and interparticle regions. The R-space spectrum of Pt-Ru/C-570 sample is consisted of Pt oxide (Pt-O1 at shell1, Pt-O2 at shell2, and Pt-PtO at shell3) and metallic PtRu alloy contributions (Pt-PtM and Pt-RuM at shell3). As expected, both the *CNs* for Pt oxide and metallic Pt (Pt-PtM) are increased indicating the severe oxidation and the sintering of NPs. In addition considering to the geometry effects on the heteroatomic *CN* for atoms at core and shell regions, the existence of Pt-RuM contribution is a clue for the presence of Pt to Ru conjunction with the Pt structure riched at shell region even in a presence of severe interparticle sintering (will be proved in ESI). From a theoretical *CN* to size correlation, the XAS determined Pt domain size is less than 1.5 nm.[52] This result seems controversial to that obtained from XRD and TEM (where Pt NPs has an average coherent length of ~3.0 nm), however could be rationalized by the high density of heteroatomic structures in Pt regions including the surface oxidation, the Pt to Ru alloy,[11, 13] and possibly the heterogeneous interface between metallic Pt domains and metal oxide region (the enclosure of Pt clusters in RuO_2 crystallites).[42] The presence of small Pt-Pt *CN* from metallic Pt structure are important indications for the high ratio of Pt atoms that exposing to surface or locating at heterogeneous interfaces. It is therefore suggested that the majority of Pt atoms are interacted with oxygen atoms to form PtO / PtO_2 clusters at the poorly crystalline Ru oxide surface. At such a structure, a substantial extent of heterogeneous contact is formed. They are strained overlayers and heterogeneous intermix; where the effect of strain and heterogeneous atomic electronic interactions (ligand effect) would participate in their electrochemical properties.

Combining the results of XANES analysis and HRTEM, the results of Pt L_3-edge EXAFS fitting disclose the significances of the *ordered interface (interphase) to the charge relocation* and thus the electrochemical performance of the Pt-Ru/C-T_o in the later sections. As shown in **Table 1**, one can notice that the Pt-Ru/C-520 performs a similar extent of oxidation but a h_{Ts} value of 1.92 which is ~15% higher than that of Pt-Ru/C-H_2. From HRTEM images, one can notice that all of the nanoparticles in Pt-Ru/C-520 are grown in faceted crystallites which projecting to the 2D images in hexagonal shape with a distinct interface in the near surface region (shown by the arrow in white). However, the nanoparticles in Pt-Ru/C-H_2 samples are mostly ellipsoid like indicating their high density of surface defects. Taking together, one can conclude that 1. By annealing at high T_o the crystallinity (i.e., the atomic ordering) of NPs will be improved; 2. such atomic ordering will reduce the surface defects and thus to a certain extent the oxidation of surface Pt atom; 3. most importantly, such atomic ordering reduces the defects of the metal to oxide heterojunction (a semi-coherent interface between Pt(111) and RuO_2 (200) facets. Note that the lattice mismatch between other facets of metallic Pt and RuO_2 are larger than 6%. These facets will form incoherent interfaces with high density of dislocation which guiding the in-plan electron diffusion and thus suppress the injection or extraction between the two phases) and thus substantially enhances the charge extraction from Pt atoms (i.e., increase the h_{Ts}).

From characterization results, a schematic representation for Pt-Ru/C-T_o could be drawn in **Scheme 1:** For freshly-prepared sample (i.e., Pt-Ru/C-H_2), the NCs comprise a Pt riched shell (denoted by **arrow A**) with a layer of oxygen absorbed Pt (denoted by **arrow B**) and the metallic Ru riched core (denoted by **arrow C**) with discrete oxidation at the interfaceted regions (**denoted by arrow D** and revealed by the broad (111) diffraction peak, the EXAFS fitting, and the previous TRP analysis).[17] By increasing T_o from 300 K till 470 K, the remaining Ru in core was progressively oxidized into hydrated amorphous Ru oxide. By further increasing T_o till 520 K, the Ru oxide was transformed into rutile phase RuO_2 (denoted by **arrow E**) and resulting in a semicoherent interface of Pt to RuO_2 heterojunction. When T_o > 520 K, the RuO_2 crystallinity would drastically been increased, which resulting in a strong lattice strain at surface Pt phase. It would substantially weaken the surface Pt-O bonding therefore facilitating the PtO_2 dissociation and the subsequent restructure of the Pt atoms into the metallic Pt clusters[36, 53]. Circumstantially, both the RuO_2 surface exposure and the formation of RuO_2@Pt junction would facilitate the carbon combustion and thus leading to the segregation between metallic Pt and RuO_2 NPs. The former is processed by the presence of Ru-O-C bonding[41] and the latter is charge extraction from Pt to their substrate (will be elucidated by the density function theory, DFT, calculation).

Calculation of surface binding energies at heterogeneous surface

Combining results of XRD, TEM, TPD-MS, and XAS analyses we know that the oxidation treatment will restructure the NCs from metallic Ru core – Pt shell structure into the structure of rutile phase Ru oxide core/Pt metal/Pt oxide shell that containing ordered metal to oxide heterojunction. The NCs with crystallite RuO_2 exposure to the surface is of important interests on fuel cell applications. By forming bonding between the RuO_2 and carbon, it shows high performance on decomposing the graphite materials (carbon support) at a temperature below 500 – 550 K[34] and thus is believed a potential candidate for improving the electrochemical oxidation of methanol. In this study according to results of TGA and TPD-MS analysis, the presented sample can even facilitate the carbon oxidation at 400 K (see **Fig. 4** and **Fig. S5**), which is about 100 to 150 K lower than that of carbon supported RuO_2 nanocomposites.[34] Therefore, it appears that an additional driving force possibly the presence of RuO_2 to Pt heterojunction participate in this reaction. This mystery can be disclosed by considering the facts of electron relocation between the catalyst and the reactants (carbon atoms). For oxidation, the facilitated reaction kinetics is attributed to the easy electron extraction from the reactants by chemisorption sites they are landed. Our results of DFT calculation, which can be seen in **Fig. 8** and **Table 2**, clarify the experimentally hypothesis where the oxygen molecules are spillover decomposed into oxygen radicals to facilitate the chemical reactions at the NCs surface with a heterojunction of metallic Pt atoms at RuO_2 rutile crystallite. From bulk heterojunction physics we know that any types of structure disorder (including vacancy, heteroatomic intermix, dislocation, and interfaceted boundary *etc.*) will hinder the electron transportation to a certain extent in a material. In addition, the effects of lattice mismatch can only propagate by less than 5 atomic layers from heterojection to the near surface region (i.e., shell). Therefore, the DFT simulation on models with experimentally obtained crystal dimensions might not easy to answer the clues. Hence, to clarify our hypothesis the electron extraction capabilities for two types of models with simplified structure (metallic Pt layer subjecting at metallic Ru (0001) substrate and rutile RuO_2 (001) (T-RuO_2)) are compared; where atomic oxygen was landed at the topmost Pt surface. For matching the local atomic environments of the Pt-Ru/C-T_o NCs, the model of rutile RuO_2 (001) facet, which possessing the inter-atomic distances identical to that of RuO_2 (002), with monolayer of Pt capping atoms is selected.

Cite this: DOI: 10.1039/c0xx00000x

www.rsc.org/xxxxxx

ARTICLE TYPE

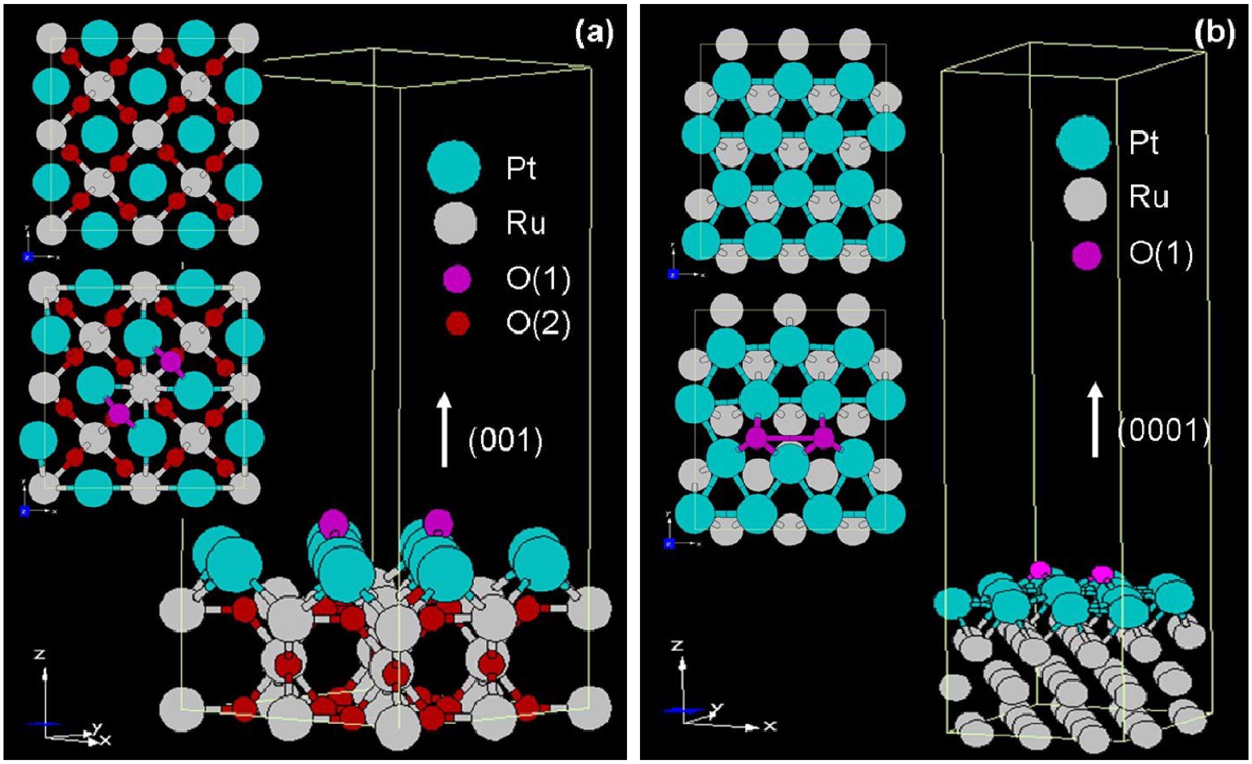

Fig. 8 Top view and side view of the simulated oxygen adsorption on (a) Pt on (001) RuO_2 and (b) Pt on (0001) Ru. Both surfaces with and without adsorbed oxygen atoms are shown at the middle left and the upper left corner of each figure, respectively. All structures have been optimized using DFT calculation. O(1) denotes the oxygen atoms belonging to the absorbed oxygen molecule while O(2) represents the oxygen atoms in the RuO_2 sublayer.

It is noted that the (001) facet of face-centered cubic Pt bulk has a lattice constant of a = 3.92 Å. Therefore, a lattice mismatch of 14.6 % between the Pt monolayer and RuO_2 sublayer induces a strong tensile lattice strain on Pt atoms that follow the (001) orientation of the RuO_2 surface. In contrast, on a surface of metallic Ru (0001) facet (a = 2.76 Å and c = 4.28 Å) Pt atoms form a hexagonal lattice with a lattice spacing of 2.755 Å analogue of that of (111) facet of a Pt bulk crystal (~2.770 Å). In such architecture, these top layer Pt atoms experience a 1.5 % compressive lattice mismatch, therefore, the binding of molecular oxygen at their surface is weakened. It is worth stressing another contrast between the two kinds of substrates that the spacing between the (001) Pt monolayer and the top layer of the (001) RuO_2 sublayer is much shorter than that between (111) Pt monolayer and the top layer of the (0001) Ru sublayer (~45.7 %) as shown in **Table 2**.

Table 2 Parameter extracted from DFT calculations. The differences of the parameters (in both percentage and absolute value) are given between two substrates considered Pt/(0001)Ru as the reference.

Parameters	Pt/(001)RuO_2	Pt/(0001)Ru	difference (%)
O absorbing position	bridge	f.c.c hallow	
Lattice mismatch (%)	14.6 (tensile)	1.5 (compressive)	16.1
O-O bond length (Å)	3.29	2.91	11.6
O-Pt bond length (Å)	1.97	2.07	-5.1
O-Pt surface distance (Å)	1.09	1.33	-22
Pt layer-to-sublayer distance (Å)	1.56	2.28	-46.2
Absorption energy (eV)	5.35	2.29	57.2

This implies that beside the effect of lattice strain on the oxygen chemisorptions, the additional ligand effect of the sublayer atoms is expected to be stronger for the (001) RuO_2 than for the (0001) Ru. Evidently, the absorption energy of the oxygen molecule on the Pt/(001)RuO_2 substrate (5.35 eV) is more than twice of that on the Pt/(0001) Ru substrate (2.29 eV). Moreover, the two oxygen atoms of the absorbed oxygen molecule are dissociated into a farther distance and come closer to the Pt surface for the case of Pt/(001)RuO_2 than for the case of Pt/(0001) Ru. Also, the oxygen atoms accommodate at the bridge positions between two Pt atoms in the former case while they sit at the f.c.c. hallow positions in the latter one. This difference in absorbing position makes the Pt-O bond length is shorter in the former than in the latter. Therefore, it is inferred from our DFT calculation that due to stronger tensile lattice strain and additional ligand effect, oxygen molecules may be dissociated more easily on Pt/RuO_2 and they may bind more strongly to the surface to form a regular oxygen atomic layer as the transition site for the subsequent spillover dissociation and diffusion of oxygen atoms when the coverage of absorbing oxygen molecules increases[53]. This surface atomic oxygen layer would subsequently interact with the carbonaceous species, consequently improving the MOR activities of 520 K treated Pt-Ru/C-T_o.[17, 30] The details of surface oxygen induced catalysis will be addressed and reported elsewhere.

Effects of annealing temperature on the electrochemical properties of Pt-Ru/C

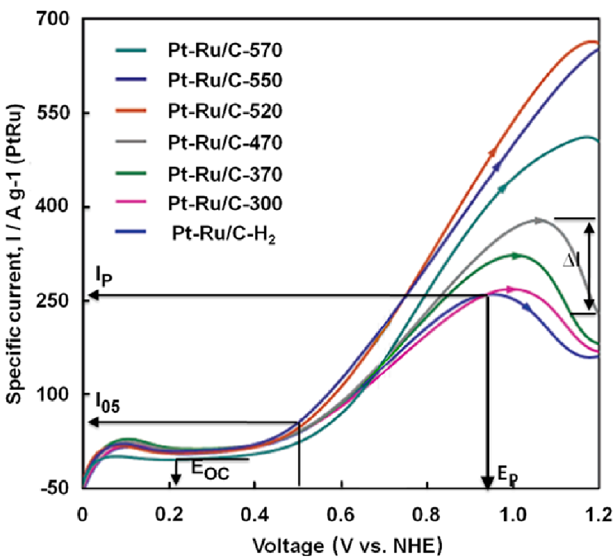

Fig. 9 The linear sweep voltammograms (LSV) of methanol oxidation on fresh (Pt-Ru/C-H_2) and Pt-Ru/C-T_o catalysts in 1.0 M CH_3OH and 0.5 M H_2SO_4. The anodic potentials were swept between 0.0 and 1.2 V (*vs.* NHE) in a rate of 20 mV s^{-1} at room temperature.

Table 3 Electrochemical performances of Pt-Ru/C catalysts

sample	I_{05} (A g^{-1} (Pt-Ru))	I_P (A g^{-1} (Pt-Ru))	E_P (V)
Pt-Ru/C-H_2	36.6	255	0.92
Pt-Ru/C-300	36.6	268	0.99
Pt-Ru/C-370	36.6	322	1.00
Pt-Ru/C-470	36.6	377	1.05
Pt-Ru/C-520	43.9	663	1.18
Pt-Ru/C-570	54.9	508	1.17

The effects of T_o on Pt-Ru/C activity over MOR were characterized by CV, and the results of anodic peak activity (I_P), the activity at the half-peak potential at 0.5 V (I_{05}), and the peak potential (E_P) are summarized in **Table 3**. The anodic LSV curves of T_o treated samples ranging from 0 to 1.2 V *vs.* NHE are compared in **Fig. 9**. In general, anodic electrooxidation of each methanol molecule releases 4 protons, 4 electrons and one carbon monoxide (CO). The released CO will passivate the surface of NCs through the reaction in the **eqn (3)**:

$$CH_3OH + * \rightarrow 4H^+ + 4e^- + * - CO \qquad (3)$$

where * denotes a Pt site on NCs surface. Hence, a catalyst with high activity for **eqn (3)** should give a high I_P at a low E_P. When the potential is higher than E_P, the current decreases sharply while other carbonaceous intermediates are possible to form, including aldehydes (-CHO^{ads}), carbonyl (-CO^{ads}), and carboxyl (-$COOH^{ads}$). All these absorbed molecules hinder the NCs surface from the subsequent adsorption and the oxidation of MeOH.[12, 13, 28, 54] In a LSV sweep spectrum, I_P may serve as the index for the electrooxidation effectiveness and onset potential E_{OC} means the applied electrochemistry force that initiates the methanol oxidation on certain electrodes (in our study the NCs on Pt-Ru/C). The current drop $\Delta I = I_P - I_{12}$ (I_{12} is the current at a potential of 1.2 V *vs*. NHE) is possibly induced by chemisorptions of carbonaceous intermediates in **eqn (4)**:

$$\begin{aligned} & Pt + CH_3OH \rightarrow Pt-(CH_3OH)^{ads} + Pt \rightarrow ... \\ & \rightarrow Pt_2-(CO)^{ads} / Pt-(CHO)^{ads} \end{aligned} \qquad (4)$$

at applied potential lower than E_P.[12, 28, 54] In the meantime, the I_{05} gives qualitative information about the amount of active Pt sites working in Pt-Ru/C under E = 0.5 V.[13] In **Fig. 9**, the Pt-Ru/C-H_2 initiates the MOR at E_{OC} ~0.21 V resulting in a I_P = 255 A per gram of metal (A g^{-1} (Pt-Ru)) at E_P = 0.92 V. The I_P of oxidized NCs were found increasing from 255 to 663 A g^{-1} (Pt-Ru), with a decreasing of ΔI from ~120 to 0 A g^{-1} (Pt-Ru), with T_o from 300 K to 520 K; where the E_{OC} is found in a similar value of ~0.16 V among all the experiments of Pt-Ru/C-T_o NCs.

Results combining above structure information (see **Scheme 1**) and electrochemical analysis clarify the mechanisms enhancing the MOR activity of NCs on Pt-Ru/C. From heterogeneous catalysis standpoints, the MOR activity of NCs depends on how their Pt sites are subjected to local and crystal structures in the near-surface regime. Since the shapes of LSV curves are found varied with T_o, the MOR should process in different pathways in accordance with the surface structures of Pt-Ru/C-T_o. The Pt-Ru/C-H_2 sample has a highest E_{OC} and lowest I_P, implies the highest surface energy barriers for MOR as consistently probed by its lowest valence charge donation and heteroatomic interaction between Pt and neighboring atoms among all samples. For Pt-Ru/C oxidized at T_o < 370 K, the Pt atoms are surrounded by mainly amorphous RuO_2 oxide and partially Ru metal. In these two cases, the Pt atoms would strongly bind with oxygen atoms, consequently resulting in the poor MOR activity. For oxidized Pt-Ru/C, more and more RuO_2 in contact with metallic Pt formed as annealing T_o increased. The RuO_2 sublayer would attract oxygen and hydroxide radicals that participating in the MOR reaction at Pt surface. Such surface sites facilitate the oxygen molecule dissociation and thus giving rise of high MOR activity (I_P) of electrocatalysts.[13, 17, 19] The 520 K sample performs the maximum I_P and minimum ΔI. From geometric point of view, since the changes of sizes and dispersions of supported NCs are small, the superior I_P (663 A g^{-1} (Pt-Ru)) with a low ΔI (~0 A g^{-1} (Pt-Ru)) value could be attributed to the strong ligand effect, lattice mismatch, and high density of heterogeneous surface sites of Pt atoms that are subjected to T-RuO_2 sublayer.[1,]

[2, 13, 15, 16, 27, 28, 55] Such results are consistently revealed by previous literatures which suggesting that the close proximity between Pt and Ru atoms by forming the heterojunction could better act the catalytically than PtRu alloy formation for the CO removal from the surface of bimetallic NCs.[56]

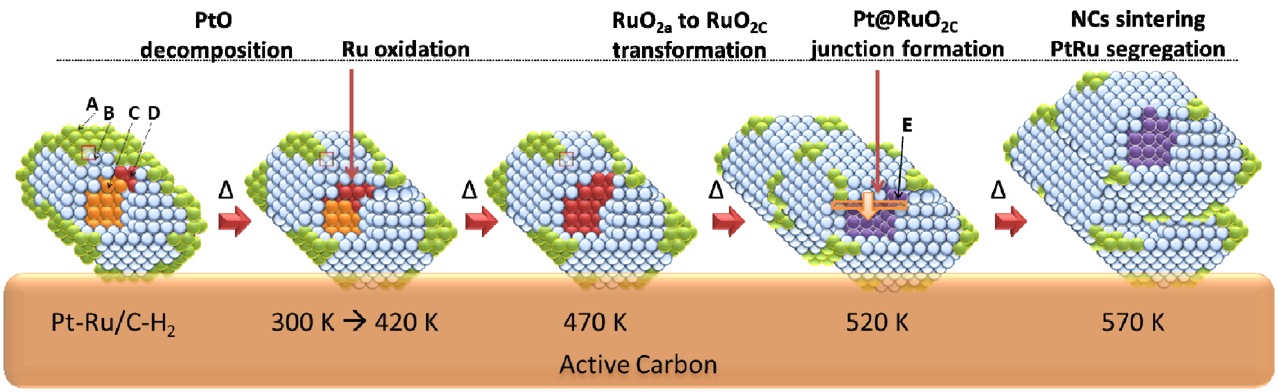

Scheme 1 Schematic representation for the structural evolutions of Pt-Ru/C catalysts after oxidized at different temperatures. A: Pt-O^{ads}; B: metallic Pt; C metallic Ru; D: amorphous Ru oxide (RuO_{2a}); E: crystalline (Rutile) RuO2 (RuO_{2C}). The arrow at heterojunction points to the electron extraction direction from Pt to RuO_{2a}.

At such Pt metal to RuO_2 heterojunction, presumably, the sublayer would extract the electrons from Pt atoms and thus facilitate the formation of oxygen chemisorptions (RuO^2@Pt-$2O^{ads}$). Hereby, the ΔI of catalysts is reduced possibly by a step that modified from **eqn (4)** "RuO_2@Pt-$2O^{ads}$ + CH_3OH --> ... --> RuO^2@Pt-O^{ads} + RuO_2@Pt-O^{ads} --> RuO_2@PtR + CO_2". In this step, the "RuO_2@Pt^{R}" denotes the retained valid site. It would rapidly been oxidized into RuO_2@Pt-$2O^{ads}$ (or hydrated into RuO_2@Pt-$2OH^{ads}$) by dissociating O_2 molecules (or attracting OH radicals). These surface radicals and chemisorptions are highly reactive to carbonaceous retentions and would regenerate the surface sites to enable the MOR reaction in high applied potential with low poisoning effects (low ΔI). From the structural characterizations we can notice that the density of empty states of Pt atoms is increased to a maximum extent at T_o = 520 K. Since the extent of heteratomic intermixes is drop to a minimum extent, it is believed that such electron extraction from Pt can be originated from the presence of ordered heterojunction instead of the bifunctional mechanisms. Hence, it is expectable to find the 520 K sample have the highest E_P and the lowest ΔI among all catalysts. For Pt-Ru/C-570, the loss of Pt surface area and Pt to Ru interface due to segregation between Pt and Ru phases and the interparticle sintering are the main reasons for their drasticly decreased MOR activity.

Conclusions

We have elucidated the mechanistic correlations between local structures and MOR activities of nanocrystallites (NCs) on Pt-Ru/C-T_o using structure characterizations (XAS, XRD, and TEM), electrochemical characterizations (LSV, TGA, and TPD-MS), and DFT calculations. Results indicate that the performances of Pt-Ru/C-T_o are dominated by the heterogeneous structures of Pt and Ru and the lattice distortion of surrounding Pt atoms. Among these factors, the heterojunction between Pt atoms and rutile RuO_2 crystallite is found to be the most important factor to determine the MOR activity of NCs on Pt-Ru/C. By adopting such effect to the surface structure, the NCs perform the optimal MOR activity after being oxidized in adequate environment (at 520 K) by formation of RuO_2@Pt heterojunction. Such enhancement could be accounted for the facilitated dissociation of oxygen and OH into radicals chemisorptions at Pt from the strong ligand and lattice strain effect of sublayer rutile RuO_2. Further increasing T_o to 570 K, the MOR activity of Pt-Ru/C was drastically been decreased by 30% due to the loss of Pt surface area and the Pt to Ru intermix as a result of segregation between Pt metal and RuO_2 phases and the interparticle sintering. Most importantly, our work combines quantitative analysis and theoretical estimation for manipulating the structural evolutions along with the MOR activity of Pt-Ru/C catalysts. Such systematic information provides convincing strategies on the design of carbon supported catalysts for conducting the cost effective fuel cell technologies with optimized electrochemical performance.

Acknowledgements

The authors would like to thank the staff of National Synchrotron Radiation Research Center (NSRRC), Hsinchu, Taiwan for the help in various synchrotron-based measurements techniques. A special thank is due to Prof. Shih-Yuan Lu and Chi-Chang Hu and their research group (Dept. of Chemical Engineering, NTHU) who helped to analyze the LSV data. T.-L. Lin and T.-Y. Chen acknowledge the financial support received from National Science Council and Atomic Energy Council mutual fund (NSC 96-2623-7-007-022-NU and NSC 97-2623-7-007-006-NU).

Notes and references

[a] *Department of Engineering and System Science, National Tsing Hua University, Hsinchu 30013, Taiwan Fax: +886 3 5728445; Tel: +886 3 5742671; E-mail: chencaeser@gmail.com; mnguyen5@wisc.edu; tllin@mx.nthu.edu.tw; chlee@mx.nthu.edu.tw*
[b] *Institute of Materials Science and Engineering, National Central University; E-mail: kuanwen.wang@gmail.com*
[c] *Department of Environmental Science and Engineering, Tunghai University, Taichung 40704, Taiwan; E-mail: ytliu@thu.edu.tw*

[d] Department of Chemical Engineering, National Tsing Hua University, Hsinchu 30013, Taiwan
[e] Department of Chemical Engineering, University of South Carolina, Columbia, SC 29208, USA

† Electronic Supplementary Information (ESI) available: The XRD analysis, TGA analysis, DFT data simulation methods, and the XAS data collection / analysis methods are enclosed. See DOI: 10.1039/b000000x/
‡ Po-Chun Huang and Yu-Ting Liu have equally contributed to this work.

1. S. Alayoglu, A. U. Nilekar, M. Mavrikakis and B. Eichhorn, *Nature Materials*, 2008, **7**, 333-338.
2. M. Watanabe and S. Motoo, *Journal of Electroanalytical Chemistry*, 1975, **60**, 267-273.
3. T. Vidakovic, M. Christov and K. Sundmacher, *Electrochimica Acta*, 2007, **52**, 5606-5613.
4. J. de Graaf, A. J. van Dillen, K. P. de Jong and D. C. Koningsberger, *Journal of Catalysis*, 2001, **203**, 307-321.
5. C. P. Hwang and C. T. Yeh, *Journal of Catalysis*, 1999, **182**, 48-55.
6. C.-S. Tsao, Y. Liu, M. Li, Y. Zhang, J. B. Leao, H.-W. Chang, M.-S. Yu and S.-H. Chen, *The Journal of Physical Chemistry Letters*, 2010, **2010**, 1569-1573.
7. C.-S. Tsao, Y.-R. Tzeng, M.-S. Yu, C.-Y. Wang, H.-H. Tseng, T.-Y. Chung, H.-C. Wu, T. Yamamoto, K. Kaneko and S.-H. Chen, *The Journal of Physical Chemistry Letters*, 2010, **1**, 1060-1063.
8. C.-S. Tsao and U.-S. Jeng, *Journal of the American Chemical Society*, 2009, **131**, 1404-1406.
9. C. I. Contescu, C. M. Brown, Y. Liu, V. V. Bhat and N. C. Gallego, *The Journal of Physical Chemistry C*, 2009, **113** 5886-5890.
10. C. Lin, T. Xu, J. Yu, Q. Ge and Z. Xiao, *The Journal of Physical Chemistry C*, 2009, **113** 8513-8517.
11. C. Roth, N. Benker, T. Buhrmester, M. Mazurek, M. Loster, H. Fuess, D. C. Koningsberger and D. E. Ramaker, *Journal of the American Chemical Society*, 2005, **127**, 14607-14615.
12. J. L. Cohen, D. J. Volpe and H. D. Abruña, *Physical Chemistry Chemical Physics*, 2007, **9**, 49-77.
13. S. Y. Huang, C. M. Chang, K. W. Wang and C. T. Yeh, *ChemPhysChem*, 2007, **8**, 1774-1777.
14. R. Kofman, P. Cheyssac, A. Aouaj, Y. Lereah, G. Deutscher, T. Bendavid, J. M. Penisson and A. Bourret, *Surface Science*, 1994, **303**, 231-246.
15. T.-Y. Chen, T.-L. Lin, T.-J. M. Luo, Y. Choi and J.-F. Lee, *ChemPhysChem*, 2010, **11**, 2383-2392.
16. S. Y. Huang, C. M. Chang and C. T. Yeh, *Journal of Catalysis*, 2006, **241**, 400-406.
17. S. Y. Huang, S. M. Chang, C. L. Lin, C. H. Chen and C. T. Yeh, *The Journal of Physical Chemistry B*, 2006, **110**, 23300-23305.
18. A. Schlapka, M. Lischka, A. Gross, U. Kasberger and P. Jakob, *Physical Review Letters*, 2003, **91**, 016101.
19. S. Y. Huang, S. M. Chang and C. T. Yeh, *The Journal of Physical Chemistry B*, 2006, **110**, 234-239.
20. M. T. M. Koper, J. J. Lukkien, A. P. J. Jansen and R. A. van Santen, *The Journal of Physical Chemistry B*, 1999, **103**, 5522-5529.
21. P. A. Korzhavyi, I. A. Abrikosov, B. Johansson, A. V. Ruban and H. L. Skriver, *Physical Review B*, 1999, **59**, 11693-11703.
22. A. V. Ruban and H. L. Skriver, *Computational Materials Science*, 1999, **15**, 119-143.
23. B. C. Han, A. V. derVen, G. Ceder and B.-J. Hwang, *Physical Review B*, 2005, **72**, 205409.
24. Y. Y. Tong, H. S. Kim, P. K. Babu, P. Waszczuk, A. Wieckowski and E. Oldfield, *Journal of the American Chemical Society*, 2002, **124**, 468-473.
25. C. Roth, N. Martz and H. Fuess, *Physical Chemistry Chemical Physics*, 2001, **3**, 315-319.
26. C. Roth, N. Benker, M. Mazurek, F. Scheiba and H. Fuess, *Applied Catalysis A: General*, 2007, **319** 81-90.
27. M. Watanabe and S. Motoo, *Journal of Electroanalytical Chemistry*, 1975, **60**, 275-283.
28. R. R. Adzic, J. Zhang, K. Sasaki, M. B. Vukmirovic, M. Shao, J. X. Wang, A. U. Nilekar, M. Mavrikakis, J. A. Valerio and F. Uribe, *Topics in Catalysis*, 2007, **46**, 249- 262.
29. M. Schmid, W. Hofer, P. Varga, P. Stoltze, K. W. Jacobsen and J. K. Norskov, *Physical Review B*, 1995, **51**, 10937-10946.
30. A. L. N. Pinheiro, M. S. Zei and G. Ertl, *Physical Chemistry Chemical Physics*, 2005 **7**, 1300-1309.
31. E. S. Steigerwalt, G. A. Deluga, D. E. Cliffel and C. M. Lukehart, *The Journal of Physical Chemistry B*, 2001, **105**, 8097-8101.
32. S. Stoupin, E. H. Chung, S. Chattopadhyay, C. U. Segre and E. S. Smotkin, *The Journal of Physical Chemistry B*, 2006, **110**, 9932-9938.
33. S. Alayoglu and B. Eichhorn, *Journal of the American Chemical Society*, 2008, **130**, 17479-17486.
34. Z. R. Cormier, H. A. Andreas and P. Zhang, *The Journal of Physical Chemistry C*, 2011, **115**, 19117-19128.
35. E. Christoffersen, P. Stoltze and J. K. Norskov, *Surface Science*, 2002, **505**, 200-214.
36. T. Bligaard and J. K. Nørskov, *Electrochimica Acta*, 2007, **52** 5512-5516.
37. T. Vidakovic, M. Christov, K. Sundmacher, K. S. Nagabhushana, W. Fei, S. Kinge and H. Bonnemann, *Electrochimica Acta*, 2007, **52**, 2277-2284.
38. A. V. Ruban, H. L. Skriver and J. K. Norskov, *Physical Review B*, 1999, **59**, 15990-16000.
39. M. A. van Hove, R. J. Koestner, P. C. Stair, J. P. Biberian, L. L. Kesmodel, I. Bartos and G. A. Somorjai, *Surface Science*, 1981, **103** 189.
40. J. G. Zhou, H. T. Fang, Y. F. Hu, T. K. Sham, C. X. Wu, M. Liu and F. Li, *The Journal of Physical Chemistry C*, 2009, **113**, 10747-10750.
41. Z. Wu, D. Wang, W. Ren, J. Zhao, G. Zhou, F. Li and H. Cheng, *Advanced Functional Materials*, 2010, **20**, 3595-3602.
42. K. Sasaki, H. Naohara, Y. Cai, Y. M. Chio, P. Liu, M. B. Vukmirovic, J. X. Wang and R. R. Adzic, *Angewandte Chemie International Edition*, 2010, **49**, 8602-8607.
43. T.-Y. Chen, I.-L. Chen, Y.-T. Liu, T.-L. Lin, P.-W. Yang, C.-Y. Wu, C.-C. Hu, T.-J. M. Luo and C.-H. Lee, *CrystEngComm*, 2013, **15** 982-994.
44. D. R. Rolison, P. L. Hagans, K. E. Swider and J. W. Long, *Langmuir* 1999, **15**, 774-779.
45. A. K. Schmid, N. C. Bartelt and R. Q. Hwang, *Science*, 2000, **290**, 1561-1564.

46. D. A. McKeown, P. L. Hagans, L. P. L. Carette, A. E. Russell, K. E. Swider and D. R. Rolison, *The Journal of Physical Chemistry B*, 1999, **103**, 4825-4832.
47. B. Zhan, M. A. White, T. Sham, J. A. Pincock, R. J. Doucet, K. V. R. Rao, K. N. Robertson and T. S. Cameron, *Journal of the American Chemical Society*, 2003, **125**, 2195-2199.
48. N. Chakroune, G. Viau, S. Ammar, L. Poul, D. Veautier, M. M. Chehimi, C. Mangeney, F. Villain and F. Fievet, *Langmuir* 2005, **21**, 6788-6796.
49. S. N. Reifsnyder, M. M. Otten, D. E. Sayers and H. H. Lamb, *The Journal of Physical Chemistry B*, 1997, **101**, 4972-4977.
50. M. Newville, *Journal of Synchrotron Radiation*, 2001, **8**, 322-324.
51. J. Zhang, D. Jiang, B. Chen, J. Zhu, L. Jiang and H. Fang, *Journal of The Electrochemical Society*, 2001, **148**, A1362-A1367.
52. M. S. Nashner, A. I. Frenkel, D. Somerville, C. W. Hills, J. R. Shapley and R. G. Nuzzo, *Journal of the American Chemical Society*, 1998, **120**, 8093-8101.
53. H. E. Hoster, M. J. Janik, M. Neurock and R. J. Behm, *Physical Chemistry Chemical Physics*, 2010, **12**, 10388-10397.
54. J. D. Newson and A. C. Riddiford, *Journal of The Electrochemical Society*, 1961, **108**, 699-706.
55. R. A. van Santen and M. Neurock, in *Molecular Heterogeneous Catalysis; A conceptual and Computational Approach*, WILEY-VCH Verlag GmbH & Co. KGaA, Weinheim, 2006, pp. 19-81.
56. F. Maillard, G.-Q. Lu, A. Wieckowski and U. Stimming, *J. Phys. Chem. B*, 2005, **109**, 16230-16243.

Table of content entry: Oxidation Triggered Atomic Restructures Enhancing the Electrooxidation Activities of Carbon Supported Platinum-Ruthenium Catalysts (Chen, T.-Y. et al.)

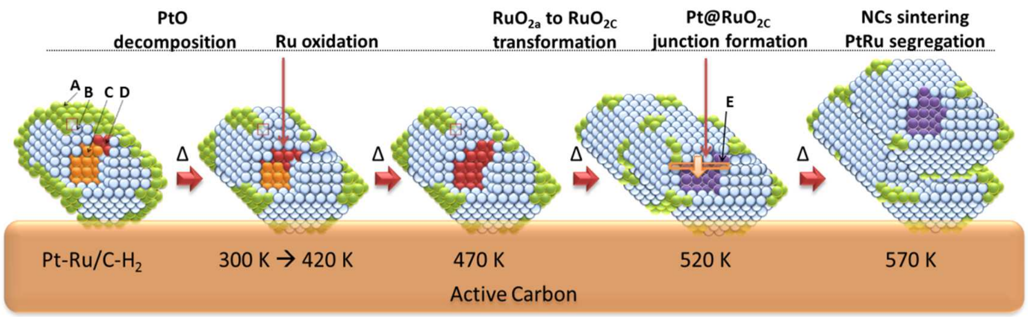

Caption: The atomic structure of carbon supported bimetallic nanocatalysts can be manipulated by oxidation treatment.